Implicit implementation and consistent tangent modulus of a viscoplastic model for polymers

Nadia Achour [a], George Chatzigeorgiou [a], Fodil Meraghni [a,*], Yves Chemisky [a], Joseph Fitoussi [b]

[a] Arts et Métiers ParisTech, LEM3-UMR 7239 CNRS, Augustin Fresnel 57078 Metz, France
[b] Arts et Métiers ParisTech, PIMM – UMR CNRS 8006, 151 Boulevard de L'Hôpital, Paris 75013, France

ARTICLE INFO

Article history:
Received 29 June 2015
Received in revised form
4 September 2015
Accepted 16 September 2015
Available online 26 September 2015

Keywords:
Polymers
Viscoplasticity
Implicit formulation
Consistent tangent modulus

ABSTRACT

In this work, the phenomenological viscoplastic DSGZ model (Duan et al., 2001 [13]), developed for glassy or semi-crystalline polymers, is numerically implemented in a three-dimensional framework, following an implicit formulation. The computational methodology is based on the radial return mapping algorithm. This implicit formulation leads to the definition of the consistent tangent modulus which permits the implementation in incremental micromechanical scale transition analysis. The extended model is validated by simulating the polypropylene thermoplastic behavior at various strain rates (from $0.92\ s^{-1}$ to $258\ s^{-1}$) and temperatures (from 20 °C to 60 °C). The model parameters for the studied material are identified using a heuristic optimization strategy based on genetic algorithm. The capabilities of the new implementation framework are illustrated by performing finite element simulations for multiaxial loading.

1. Introduction

Semi crystalline polymers are well known to exhibit a rate and temperature dependent behavior. With the increase interest for this kind of materials, in particular in the automotive industry, many phenomenological models have been developed [29,5,10,21,12,16,23,3,36,4,1] in order to take into account these properties. Many studies have also been performed to identify the evolution of damage in polymers and polymeric composites [25,26,37,2].

Several researches have proposed models to account for the viscoplastic behavior of polymers and they have developed appropriate implementation techniques for numerical calculations [32,28,31]. Some of the modeling efforts are focusing on semi-crystalline [39], glassy [35] or amorphous polymers [15].

Among the modeling efforts, the DSGZ model developed initially by [13] shows very interesting features and capabilities for viscoplasticity of polymers. Indeed, the DSGZ formulation is based on four previous models and it is able to trace different types of polymer behavior as the yielding and the hardening or softening of polymers.

Its initial one-dimensional form has been extended in 3 dimensions and implemented numerically following an explicit formulation [14]. The purpose of this paper is to propose for the first time a new, numerically implicit, formulation of the three-dimensional DSGZ phenomenological viscoplastic model and to implement it in the finite element software ABAQUS. Such an implementation allows us to use the DSGZ model as a constitutive model for matrix material in an incremental micromechanical analysis of glass fiber reinforced thermoplastic composites. Indeed, such homogenization schemes require the expression of the tangent modulus. This requirement is fulfilled using an implicit numerical integration scheme to compute the consistent tangent modulus at every step of the analysis by integrating the strain rate and the temperature effect on the matrix.

To perform numerical studies, appropriate DSGZ model parameters are identified experimentally on a thermoplastic material, namely polypropylene (PP), at different strain rates and temperatures. Certain methodologies have been proposed in the literature to identify viscoelastic/viscoplastic material parameters for polymers [22,40]. In this work, the parameter identification is achieved using a genetic algorithm coupled to gradient-based methods, which was applied successfully for shape memory alloys [34,8]. The experimental identification and validation of the model are based on thermomechanical tensile tests. Then its capability to simulate multiaxial loading is demonstrated.

* Corresponding author. Tel.: +33 387375459; fax: +33 387374284.
E-mail address: fodil.meraghni@ensam.eu (F. Meraghni).

This paper is structured as follows: the first part is dedicated to a brief reminder of the background of this interesting model. The second part presents the numerical implicit formulation and the computation of the consistent tangent modulus, allowing the formulation of an algorithm for the finite element code ABAQUS. The next part focuses on two aspects: the identification of the model parameters for polypropylene material (PP) and the experimental validation by comparison with stress–strain curves obtained at different strain rates and temperatures. The fourth part of this paper is devoted to the application of the model by simulating multiaxial tensile-shear loading cases. These simulations are performed for 6 strain rates and 3 temperatures. Finally, the last part is dedicated to the application of the model on a dynamic load simulation. The aim of this part is to illustrate the capability of the implemented implicit model to be utilized for structural FE analysis.

2. DSGZ model background

The DSGZ is a viscoplastic phenomenological model developed for glassy or semi-crystalline polymers. It has the advantage to take into account the effect of the strain ε, the strain rate $\dot{\varepsilon}$, the temperature T, the softening and the hardening. According to the initial DSGZ constitutive law, the stress, σ, is given by

$$\sigma(\varepsilon,\dot{\varepsilon},T)=K[\mathbb{f}(\varepsilon)+[\mathbb{q}(\varepsilon,\dot{\varepsilon},T)-\mathbb{f}(\varepsilon)]\mathbb{r}(\varepsilon,\dot{\varepsilon},T)]\mathbb{h}(\dot{\varepsilon},T), \tag{1}$$

with

$$\mathbb{f}(\varepsilon)=\left[e^{-C_1\varepsilon}+\varepsilon^{C_2}\right]\left[1-e^{-\alpha\varepsilon}\right],\quad \mathbb{h}(\dot{\varepsilon},T)=\dot{\varepsilon}^m e^{a/T},$$

$$\mathbb{q}(\varepsilon,\dot{\varepsilon},T)=\frac{\varepsilon e^{\left[1-(\varepsilon/C_3\mathbb{h}(\dot{\varepsilon},T))\right]}}{C_3\mathbb{h}(\dot{\varepsilon},T)},\quad \mathbb{r}(\varepsilon,\dot{\varepsilon},T)=e^{\left[\ln(\mathbb{h}(\dot{\varepsilon},T))-C_4\right]\varepsilon}, \tag{2}$$

where K, C_1, C_2, C_3, C_4, a, α and m are the model constants.

Eq. (1) is based on four previously developed models, namely the Johnson–Cook, the G'Sell–Jonas, the Matsuoka, and the Brooks models. The model proposed by [6] is a constitutive law for dynamically recrystallizable materials. DSGZ model adopts a similar structure to Brooks model but the functions $\mathbb{f}$, $\mathbb{q}$, $\mathbb{h}$ and $\mathbb{r}$ are different. G'Sell and Jonas [17] developed a phenomenological model for semi-crystalline polymers, which has the advantage of integrating the effects of viscoelasticity and viscoplasticity in a single equation. This aspect is taken into account in the DSGZ model through the term $\mathbb{h}(\dot{\varepsilon},T)$. Johnson and Cook [27] proposed a simple model to describe the plastic behavior of ductile materials. Such behavior is integrated in Eq. (1) using the term $\mathbb{f}$. Finally, Matsuoka model [7] describes the behavior of glassy polymers. It includes the effects of nonlinear viscoelasticity, elasticity and the softening, but it does not account properly large deformations mechanisms. The authors of the DSGZ model used a simplified form of Matsuoka model to describe the behavior jump exhibited at the yield point of glassy polymers.

It is worth mentioning that the main purpose of the present paper is to provide a numerical formulation of a proper viscoplastic model for polymers and the inherent tangent modulus computation. Hence, the DSGZ model is chosen here as an illustrative implementation example. Further details and insights about the mathematical formulation of the model (in particular the strain rate, strain and temperature sensitivities of functions $\mathbb{f}$, $\mathbb{q}$, $\mathbb{h}$ and $\mathbb{r}$) and material parameters K, C_1 to C_4, a and α can be found in [13,14].

3. 3D extension of the constitutive model

The one-dimensional version of the DSGZ model has been extended to 3D by the same authors [14]. In this section the essential points of the three-dimensional version are discussed.

In elasto-plasticity and elasto-viscoplasticity, it is customary to separate the strain tensor, $\boldsymbol{\varepsilon}$, into an elastic, $\boldsymbol{\varepsilon}^e$, and a plastic, $\boldsymbol{\varepsilon}^p$, contribution and also to connect the stress tensor $\boldsymbol{\sigma}$ and the elastic strain through the Hooke's law. In many cases, the nonlinear nature of these materials motivates us to write these kinds of relations in incremental or rate form [9], i.e.

$$\dot{\boldsymbol{\varepsilon}}=\dot{\boldsymbol{\varepsilon}}^e+\dot{\boldsymbol{\varepsilon}}^p, \tag{3}$$

$$\dot{\boldsymbol{\sigma}}=\boldsymbol{\mathcal{C}}:[\dot{\boldsymbol{\varepsilon}}-\dot{\boldsymbol{\varepsilon}}^p], \tag{4}$$

where $\boldsymbol{\mathcal{C}}$ denotes the fourth order elastic stiffness tensor. This formalism has two significant advantages:

1. It allows easier numerical implementation, since any computational scheme in elasto-plasticity and elasto-viscoplasticity requires iterative solution (for instance, a return mapping algorithm based on an elastic trial stress) and incremental application of the applied loading.
2. The rate form is applicable not only in small deformation processes but also in large strain problems. Many experimental results in elasto-plastic materials are expressed in true (Cauchy) stress versus true (logarithmic) strain. The expressions (3) and (4) are very common in the case of hypoelastic materials, where the $\dot{\boldsymbol{\sigma}}$ denotes an objective stress rate and $\dot{\boldsymbol{\varepsilon}}$ is the rate of deformation [30]. Thus, the formulation (3) and (4) can be used for the DSGZ model [13], which has been developed considering large deformation processes.

When considering isotropic behavior for the elastic part, Eq. (4) can be expressed as

$$\dot{\boldsymbol{\sigma}}=2\mu[\dot{\boldsymbol{\varepsilon}}-\dot{\boldsymbol{\varepsilon}}^p]+\left[\kappa-\tfrac{2}{3}\mu\right]\mathrm{tr}\dot{\boldsymbol{\varepsilon}}\boldsymbol{I}, \tag{5}$$

where $\mathrm{tr}\{\bullet\}$ denotes the trace of a second order tensor, $\boldsymbol{I}$ is the second order identity tensor, μ is the shear modulus and κ is the bulk modulus. Alternatively, using Eq. (5), the deviatoric parts of the stress and the strain

$$\boldsymbol{s}=\boldsymbol{\sigma}-\tfrac{1}{3}\mathrm{tr}\boldsymbol{\sigma}\boldsymbol{I},\quad \boldsymbol{e}=\boldsymbol{\varepsilon}-\tfrac{1}{3}\mathrm{tr}\boldsymbol{\varepsilon}\boldsymbol{I}, \tag{6}$$

are connected, in a rate form, using the following relation:

$$\dot{\boldsymbol{s}}=2\mu[\dot{\boldsymbol{e}}-\dot{\boldsymbol{\varepsilon}}^p]. \tag{7}$$

The rate of plastic strains is defined by a relation of the form

$$\dot{\boldsymbol{\varepsilon}}^p=\dot{p}\boldsymbol{\Lambda}^p, \tag{8}$$

where $\dot{p}=\sqrt{2/3[\dot{\boldsymbol{\varepsilon}}^p:\dot{\boldsymbol{\varepsilon}}^p]}$ and $\boldsymbol{\Lambda}^p$ defines the direction of the plastic flow. In classical J_2 viscoplasticity, the direction tensor is given by

$$\boldsymbol{\Lambda}^p=\frac{3}{2}\frac{\boldsymbol{s}}{\overline{\sigma}}. \tag{9}$$

The scalar quantity $\overline{\sigma}$ denotes the *Mises equivalent stress*, given as the second invariant of $\boldsymbol{s}$ per $\overline{\sigma}=\sqrt{3/2[\boldsymbol{s}:\boldsymbol{s}]}$. The DSGZ model assumes for the yield criterion[1]

$$\Phi^p(\boldsymbol{\sigma},p,\dot{p},T)=\overline{\sigma}-\sigma_y(p,\dot{p},T)\le 0, \tag{10}$$

where σ_y is provided by (11) by substituting the strain and strain rate with p and $\dot{p}$ correspondingly

$$\sigma_y(p,\dot{p},T)=K[\mathbb{f}(p)+[\mathbb{q}(p,\dot{p},T)-\mathbb{f}(p)]\mathbb{r}(p,\dot{p},T)]\mathbb{h}(\dot{p},T), \tag{11}$$

[1] In the extended version of the model [14], the authors included the hydrostatic pressure in the yield criterion. In such case a generally formulated requirement $\Phi^p(\boldsymbol{\sigma},p,\dot{p},T)\le 0$ is needed.

with

$$\mathbb{f}(p)=\left[e^{-C_1 p}+p^{C_2}\right]\left[1-e^{-\alpha p}\right],\quad \mathbb{h}(\dot{p},T)=\dot{p}^{m}e^{a/T},$$
$$\mathbb{q}(p,\dot{p},T)=\frac{pe^{\left[1-(p/C_3\mathbb{h}(\dot{p},T))\right]}}{C_3\mathbb{h}(\dot{p},T)},\quad \mathbb{r}(p,\dot{p},T)=e^{\left[\ln(\mathbb{h}(\dot{p},T))-C_4\right]p}. \tag{12}$$

4. Implicit numerical implementation

The numerical procedure discussed herein considers isothermal processes. In the case of coupled thermomechanical loading, one should also consider thermal strain and the correlation between thermal and mechanical energy through the first law of thermodynamics.

The computational implementation of a nonlinear material in a structure and the numerical solution through a finite element framework is usually based on the strain-driven *return mapping algorithm* [38]. The procedure is described as follows:

1. In the first step, the plastic strains are considered not to evolve and only generation of elastic strains occurs (*elastic prediction* step). Thus, during this step the strain increment provided by the finite element analysis is assumed to be elastic ($\dot{\boldsymbol{\varepsilon}}=\dot{\boldsymbol{\varepsilon}}^{e}$).
2. In the second step, the total strain is assumed fixed, and the error in the stress is corrected by developing plastic strains (*plastic correction* step). Thus, during this step $\dot{\boldsymbol{\varepsilon}}^{p}=\dot{p}\boldsymbol{\Lambda}^{p}$.

The second step requires the numerical integration of the evolution equations for the plastic strains and the identification of the tangent modulus that is necessary for the finite element framework. Different implementation methodologies exist, and several of these are discussed in detail in the literature of nonlinear materials (see for instance [38] for plastic and viscoplastic materials, or [41,19] for shape memory alloys). For generally anisotropic material response, one could implement either the convex cutting plane or the closest point projection algorithm. Here, due to the isotropic material behavior, the *radial return mapping* is utilized for the DSGZ model. This algorithm is robust, efficient and provides the consistent tangent modulus [43].

4.1. Preliminaries

In a backward Euler fully implicit numerical scheme, the value of a given quantity x is updated from the previous time step n to the current $n+1$ per $x^{(n+1)}=x^{(n)}+\Delta x^{(n+1)}$. Such an implicit relation is usually solved iteratively, and the current value is updated for each iteration by $x^{(n+1)(k+1)}=x^{(n+1)(k)}+\delta x^{(n+1)(k)}$ until $x^{(n+1)}$ has converged. Obviously $\Delta x^{(n+1)(k+1)}=\Delta x^{(n+1)(k)}+\delta x^{(n+1)(k)}$.

Using the Backward Euler framework, Eq. (4) is written in incremental form at time step $n+1$ as

$$\Delta\boldsymbol{\sigma}^{(n+1)}=\boldsymbol{\mathcal{C}}:\left[\Delta\boldsymbol{\varepsilon}^{(n+1)}-\Delta\boldsymbol{\varepsilon}^{p(n+1)}\right]. \tag{13}$$

In an incremental-iterative form, the plastic prediction step states that the stress during the current loading increment $n+1$ and at the end of each iteration $k+1$ is given as

$$\boldsymbol{\sigma}^{(n+1)(k+1)}=\boldsymbol{\sigma}^{(n)}+\boldsymbol{\mathcal{C}}:\left[\Delta\boldsymbol{\varepsilon}^{(n+1)}-\Delta\boldsymbol{\varepsilon}^{p(n+1)(k+1)}\right]. \tag{14}$$

In the above expression, it is worth noticing that during the plastic prediction step the iteration increment $(k+1)$ of the total strain does not evolve. Recall that for each loading step, the time increments $(n+1)$ of the total strain and temperature are supplied by the global solver and are thus known. This means that during the iterative correction, the total current strain and the temperature are kept constant, i.e.

$$\delta\boldsymbol{\varepsilon}^{(n+1)(k)}=\mathbf{0},\quad \delta T^{(n+1)(k)}=0. \tag{15}$$

It is the role of the plastic prediction algorithm to find the current stress, which may require the integration of the evolution Eq. (8) for $\boldsymbol{\varepsilon}^{p}$. If Eq. (10) is satisfied for null effective plastic strain rate, the elastic solution given by the elastic prediction step is accepted as correct and is returned to the global finite element solver for the next time increment. However, if this is not the case, evolution of the applicable inelastic internal variables via the plastic prediction is needed. The process completes when Φ^{p} is sufficiently close to zero.

The scalar-valued internal variable upon which the return mapping algorithm is based is iteratively written as

$$\begin{aligned}&\dot{p}^{(n+1)(k+1)}=\dot{p}^{(n+1)(k)}+\delta\dot{p}^{(n+1)(k)},\\&\delta p^{(n+1)(k)}=\delta\dot{p}^{(n+1)(k)}\Delta t,\\&\Delta p^{(n+1)(k+1)}=\dot{p}^{(n+1)(k+1)}\Delta t=\Delta p^{(n+1)(k)}+\delta\dot{p}^{(n+1)(k)}\Delta t,\end{aligned} \tag{16}$$

where Δt is the increment of time.

4.2. Radial return mapping

Using the backward Euler method, the necessary system of equations for the plastic prediction at time step $n+1$ is written as

$$\begin{aligned}&\Delta p^{(n+1)}=\dot{p}^{(n+1)}\Delta t,\quad \Lambda^{p}=\frac{3}{2}\eta,\\&\Delta\boldsymbol{\varepsilon}^{p(n+1)}=\frac{3}{2}\dot{p}^{(n+1)}\Delta t\boldsymbol{\eta}^{(n+1)},\quad \boldsymbol{\eta}^{(n+1)}=\frac{\boldsymbol{s}^{(n+1)}}{\overline{\sigma}^{(n+1)}},\\&\Delta\boldsymbol{s}^{(n+1)}=2\mu\left[\Delta\boldsymbol{e}^{(n+1)}-\Delta\boldsymbol{\varepsilon}^{p(n+1)}\right],\\&\Delta\boldsymbol{\sigma}^{(n+1)}=\Delta\boldsymbol{s}^{(n+1)}+\kappa\mathrm{tr}(\Delta\boldsymbol{\varepsilon}^{(n+1)})\boldsymbol{I},\\&\Phi^{p(n+1)}=\overline{\sigma}^{(n+1)}-\sigma_y^{(n+1)}\le 0.\end{aligned} \tag{17}$$

In order to solve numerically Eqs. (17), the *known* trial quantities

$$\Delta\boldsymbol{s}^{\mathrm{trial}(n+1)}=2\mu\Delta\boldsymbol{e}^{(n+1)},\quad \Delta\boldsymbol{\sigma}^{\mathrm{trial}(n+1)}=\Delta\boldsymbol{s}^{\mathrm{trial}(n+1)}+\kappa\mathrm{tr}(\Delta\boldsymbol{\varepsilon}^{(n+1)})\boldsymbol{I}, \tag{18}$$

and

$$\Phi^{p\mathrm{trial}(n+1)}=\sqrt{\frac{3}{2}[\boldsymbol{s}^{\mathrm{trial}(n+1)}:\boldsymbol{s}^{\mathrm{trial}(n+1)}]}-\sigma_y^{(n)}=\overline{\sigma}^{\mathrm{trial}(n+1)}-\sigma_y^{(n)}, \tag{19}$$

are defined. Combining Eqs. (17) and (18) and given that $\boldsymbol{s}^{\mathrm{trial}(n)}=\boldsymbol{s}^{(n)}$ and $\boldsymbol{\sigma}^{\mathrm{trial}(n)}=\boldsymbol{\sigma}^{(n)}$, it can be easily demonstrated that

$$\begin{aligned}\boldsymbol{s}^{\mathrm{trial}(n+1)}&=\boldsymbol{s}^{(n)}+2\mu\Delta\boldsymbol{e}^{(n+1)}=\boldsymbol{s}^{(n+1)}+2\mu\Delta\boldsymbol{\varepsilon}^{p(n+1)}\\&=\left[\overline{\sigma}^{(n+1)}+3\mu\dot{p}^{(n+1)}\Delta t\right]\boldsymbol{\eta}^{(n+1)},\\\boldsymbol{\sigma}^{(n+1)}&=\boldsymbol{\sigma}^{\mathrm{trial}(n+1)}-3\mu\dot{p}^{(n+1)}\Delta t\boldsymbol{\eta}^{(n+1)}.\end{aligned} \tag{20}$$

From (20) and (17), it becomes clear that $\boldsymbol{s}^{\mathrm{trial}(n+1)}$ and $\boldsymbol{s}^{(n+1)}$ have the same direction. This leads to the identification of $\boldsymbol{\eta}^{(n+1)}$ as

$$\boldsymbol{\eta}^{(n+1)}=\frac{\boldsymbol{s}^{\mathrm{trial}(n+1)}}{\overline{\sigma}^{\mathrm{trial}(n+1)}}, \tag{21}$$

where

$$\overline{\sigma}^{\mathrm{trial}(n+1)}=\overline{\sigma}^{(n+1)}+3\mu\dot{p}^{(n+1)}\Delta t. \tag{22}$$

When plastic strains are developed, $\Phi^{p(n+1)}=0$. Using Eq. (22), the yield criterion and the evolution equation presented in (17) produce the nonlinear system of equations

$$\begin{aligned}&\Phi^{p(n+1)}=\overline{\sigma}^{\mathrm{trial}(n+1)}-3\mu\dot{p}^{(n+1)}\Delta t-\sigma_y^{(n+1)}=0,\\&p^{(n+1)}=p^{(n)}+\dot{p}^{(n+1)}\Delta t.\end{aligned} \tag{23}$$

Eqs. (23) are solved using the Newton–Raphson scheme. In the Newton–Raphson an additional incremental step m^{*} is introduced

and the equation

$$\dot{p}^{(n+1)(m^*+1)}\Delta t = \dot{p}^{(n+1)(m^*)}\Delta t - \frac{\Phi^{p(n+1)(m^*)}}{\Phi^{p'(n+1)(m^*)}},$$

with

$$\Phi^{p(n+1)(m^*)} = \overline{\sigma}^{\text{trial}(n+1)} - 3\mu\dot{p}^{(n+1)(m^*)}\Delta t - \sigma_y^{(n+1)(m^*)},$$

$$\Phi^{p'(n+1)(m^*)} = \frac{1}{\Delta t}\frac{\partial \Phi^{p(n+1)(m^*)}}{\partial \dot{p}^{(n+1)(m^*)}} = -\left[3\mu + h^{(n+1)(m^*)}\right],$$

and

$$h^{(n+1)(m^*)} = \frac{\partial \sigma_y^{(n+1)(m^*)}}{\partial p^{(n+1)(m^*)}} + \frac{\partial \sigma_y^{(n+1)(m^*)}}{\partial \dot{p}^{(n+1)(m^*)}}\frac{1}{\Delta t},$$

is solved iteratively. The internal variable p is also updated at each increment, using the formula

$$p^{(n+1)(m^*+1)} = p^{(n)} + \dot{p}^{(n+1)(m^*+1)}\Delta t.$$

When $|\Phi^{p(n+1)(m^*)}|$ is less than a tolerance the iterative scheme ends, the stresses are computed from $(20)_2$ and the plastic strains from the relation

$$\boldsymbol{\varepsilon}^{p(n+1)} = \boldsymbol{\varepsilon}^{p(n)} + \tfrac{3}{2}\dot{p}^{(n+1)}\Delta t\boldsymbol{\eta}^{(n+1)}.$$

4.3. Consistent tangent modulus

The consistent elasto-viscoplastic tangent modulus is now computed by linearizing the return mapping algorithm detailed in the previous subsection. At time $n+1$ it can be shown [11] that

$$\frac{\partial \Delta\boldsymbol{\sigma}^{(n+1)}}{\partial \Delta\boldsymbol{\varepsilon}^{(n+1)}} = \lambda^*\boldsymbol{I}\otimes\boldsymbol{I} + \mu^*\left[\overline{\boldsymbol{I}\otimes\boldsymbol{I}} + \underline{\boldsymbol{I}\otimes\boldsymbol{I}}\right] + \left[\frac{h}{1+\dfrac{h}{3\mu}} - 3\mu^*\right]\boldsymbol{\eta}^{(n+1)}\otimes\boldsymbol{\eta}^{(n+1)}, \tag{24}$$

with

$$\mu^* = \mu\frac{\sigma_y^{(n+1)}}{\overline{\sigma}^{\text{trial}(n+1)}}, \quad \lambda^* = \kappa - \frac{2}{3}\mu^*, \quad h = \frac{\partial \sigma_y^{(n+1)}}{\partial p^{(n+1)}} + \frac{\partial \sigma_y^{(n+1)}}{\partial \dot{p}^{(n+1)}}\frac{1}{\Delta t}. \tag{25}$$

Moreover, the symbols $\boldsymbol{I}\overline{\otimes}\boldsymbol{I}$ and $\boldsymbol{I}\underline{\otimes}\boldsymbol{I}$ are fourth order tensors and express the two special dyadic products of the identity tensor, defined in indicial notation as

$$[\boldsymbol{I}\overline{\otimes}\boldsymbol{I}]_{ijkl} = \delta_{ik}\delta_{jl}, \quad [\boldsymbol{I}\underline{\otimes}\boldsymbol{I}]_{ijkl} = \delta_{il}\delta_{jk}, \tag{26}$$

where δ_{ij} is the Kronecker delta tensor. Details on the derivation of (24) are given in Appendix A. The computational algorithm for the radial return mapping is provided in Table 1.[2]

In the described algorithm, the derivatives of the yield stress σ_y with regard to the scalar plastic quantities p and $\dot{p}$ are required. For the DSGZ model given by (11), these derivatives are expressed as

$$\frac{\partial \sigma_y}{\partial p} = K\left[\frac{\partial \mathbb{f}}{\partial p} + \left[\frac{\mathbb{q}}{p} - \frac{\mathbb{q}}{C_3\mathbb{h}} - \frac{\partial \mathbb{f}}{\partial p}\right]\mathbb{r} + [\mathbb{q} - \mathbb{f}]\frac{\mathbb{r}}{p}\ln\mathbb{r}\right]\mathbb{h},$$
$$\frac{\partial \sigma_y}{\partial \dot{p}} = \frac{Km}{\dot{p}}\left[\mathbb{q}\left[\frac{p}{C_3\mathbb{h}} - 1 + p\right] - \mathbb{f}p\right]\mathbb{r}\mathbb{h} + \frac{m\overline{\sigma}}{\dot{p}}, \tag{27}$$

where

$$\frac{\partial \mathbb{f}}{p} = \left[-C_1e^{-C_1p} + C_2p^{C_2-1}\right]\left[1 - e^{-\alpha p}\right] + \left[e^{-C_1p} + p^{C_2}\right]\alpha e^{-\alpha p}. \tag{28}$$

[2] For the consideration of large structural rotations, the discussion of [24,20] in the case of shape memory alloys is applicable. In this case, a computation is added at the third step in Table 1, in which the tensorial internal variables (i.e. the elastic and plastic strains) are properly rotated into a current reference frame for each loading step, using a rotator tensor $\mathcal{Q}$.

Table 1
Return mapping algorithm (radial return mapping) for the DSGZ model.

(1) At time n all the quantities are known.
(2) At time $n+1$ use the equilibrium equations and the constitutive relations to identify the total strains $\varepsilon^{(n+1)}$.
(3) Compute the elastic stiffness tensor, the trial stresses $\sigma^{\text{trial}(n+1)}$, the trial elastic strains $\varepsilon^{e\ \text{trial}(n+1)} = \varepsilon^{e(n)} + \Delta\varepsilon^{(n+1)}$ and the trial plastic strains $\varepsilon^{p\ \text{trial}(n+1)} = \varepsilon^{p(n)}$.
(4) Check the trial yield criterion $\Phi^{p\ \text{trial}(n+1)}$.
If $\Phi^{p\ \text{trial}(n+1)} \le 0$, exit.
If $\Phi^{p\ \text{trial}(n+1)} > 0$, proceed to the next step.
(5) (a) Initialize by setting $\dot{p}^{(n+1)(0)} = \dot{p}^{(n)}$.
(b) Identify $\dot{p}^{(n+1)(m^*+1)}\Delta t$ and update $p^{(n+1)(m^*+1)}$.
(c) Evaluate $\sigma_y^{(n+1)(m^*+1)}$ and its derivatives with respect to p and $\dot{p}$.
(d) If $|\Phi^{p(n+1)(m^*)}| < \text{tol}$ then proceed to step 6, else set $m^* = m^*+1$ and return to b.
(6) Update the elastic strains, the plastic strains and the stresses.
(7) Compute the consistent elasto-viscoplastic tangent modulus.

Remark The numerical stability of the radial return mapping algorithm is guaranteed if the yield criterion Φ^p is convex with regard to its arguments [43]. In the DSGZ model however the convexity could not be ensured for specific choice of material parameters. Nevertheless, in all the analyses performed in this work no numerical convergence issues raised.

5. Experimental identification and validation for polypropylene material

The radial return mapping algorithm presented above has been implemented in the finite element program ABAQUS standard using a user defined subroutine UMAT (details for developing such routines can be found in [42]).

Experimental tensile tests have been performed to identify the model parameters. Simulations with the developed ABAQUS subroutine are compared with the experimental tests and with the analytical results using the 1-D model.

5.1. Experimental procedure and material description

Tensile tests at different strain rates and temperatures were conducted upon a servo hydraulic test machine on a thermoplastic polymer, namely polypropylene, which has glass transition temperature $T_g = 0\,^\circ\text{C}$ and Young modulus at room temperature $E = 1680$ MPa. The high-speed test machine can reach a crosshead speed range from $10^{-3}\,\text{m s}^{-1}$ (quasi-static) to $20\,\text{m s}^{-1}$. A high speed camera (FASTCAM-APX RS), with the capacity 250,000 frames per second, is utilized to follow the deformation of the specimens surface. Strain is measured using the high speed camera through a contactless technique: two points are marked on the surface of the specimens defining the initial gauge length which is about 10 mm. Image analysis is then performed in order to follow the displacement of the centroid of each marker point and compute the evolution of the strain between these two points. Using the procedure described in [33], the true (Cauchy) stress and true (logarithmic) strain can be determined by the engineering stress, σ_n, and strain, ε_n, respectively as follows:

$$\varepsilon = \ln(1+\varepsilon_n), \quad \sigma = \sigma_n(1+\varepsilon_n). \tag{29}$$

Additionally, strain rate can be easily determined from the slope of the linear part of the strain evolution vs. time diagram. The dimensions of the test specimens used are shown in Fig. 1.

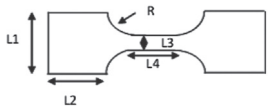

L1(mm)	L2(mm)	L3(mm)	R(mm)	L4(mm)	Thickness (mm)
15	15	5	12	10	2.8

Fig. 1. Specimens dimensions.

Table 2
Parameter values identified by the Matlab genetic algorithm.

C_1 (–)	C_2 (–)	α (–)	m (–)	a [Kelvin]	K (MPa s^m)	$C_3(s^m)$	C_4 (–)
0.435	1.661	201.926	0.056	1085.935	0.84	0.1	94.863

5.1.1. Experimental identification

The model has 8 material parameters. These parameters can be obtained by two ways:

- By exploiting specific points on 3 different stress-strain curves of tensile tests as presented in [13].
- By identifying through an optimization method.

In this study, the material parameters are identified by an inverse method based on a Matlab routine that utilizes a genetic algorithm coupled with the Levenberg–Marquart algorithm [8]. The principal advantage of using this algorithm is to avoid local minima.

The considered cost function is expressed as follows:

$$C(p) = \frac{\sum_{i=1}^{np} (\sigma_{th}^i(p) - \sigma_{exp}^i)^2}{\sum_{i=1}^{np} (\sigma_{exp}^i)^2} \tag{30}$$

where σ_{th} and σ_{exp} are the theoretical and the experimental stress respectively. (p) is the parameter vector to be identified and (np) is the number of experimental data. The identification procedure exploits all the experimental points (200 points for each stress-strain curve) in the plastic regime of three stress-strain curves corresponding to quasi-static and high speed tensile tests performed at two different temperatures (20 °C and 60 °C) and three different strain rates (0.92 s^{-1}, 24.5 s^{-1} and 64.77 s^{-1}). In this work, all part of the $\sigma - \epsilon$ curve are considered to be of equal importance. Table 2 summarizes the identified parameters.

With the increase of the engineering strain, a drop on the engineering stress is observed after the maximum stress, which is attributed to the reduction of the specimen cross-section. Under the assumption of material incompressibility due to viscoplastic strains, this overall phenomenon is corrected by using the true stress and true strain expressions (29). Nevertheless, during the performed experiments, up to 0.3 strain level, no localization in the deformation occurred. For larger strain levels, where local necking is important, a different approach needs to be followed for estimating the true stress–strain curve (see for instance [17,18] for cylindrical specimens).

In Fig. 2, simulated curves obtained for several strain rates and temperatures are compared to the corresponding ones from analytical 1D calculations and experiments.

The analytical results agree well with the simulated ones from the ABAQUS computations using the proposed implicit implementation. Moreover, the simulations show good agreement with the experimental results. Nevertheless, for higher strain rates or at lower temperatures, an overshot appears experimentally in the transition between the elastic and the plastic regime. This stress–strain transition after yielding is not considered properly by the numerical simulation. However, in the worst case, the maximum

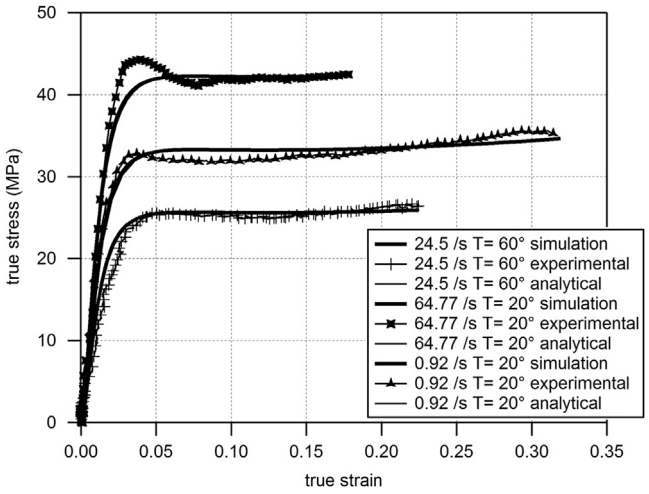

Fig. 2. Comparison between experiments utilized for material parameters identification, analytical calculations and numerical simulations.

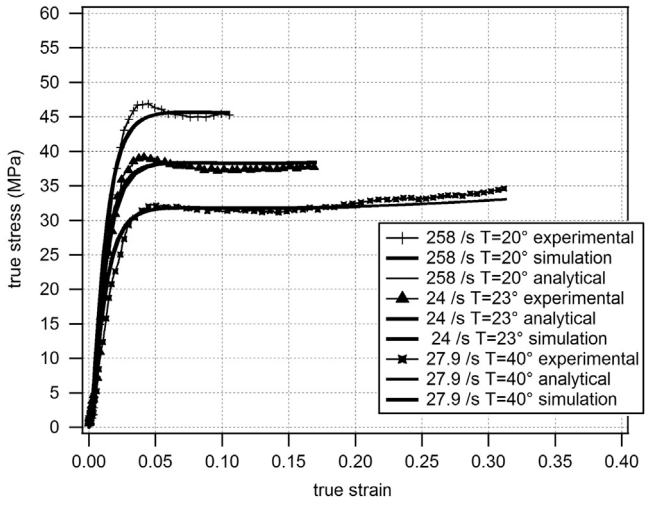

Fig. 3. Model validation through the comparison between additional experiments, analytical calculations and numerical simulations.

relative difference between experimental and simulated curves does not exceed 8% in terms of stress. The DSGZ model is fundamentally able to capture the softening after yielding for semi-crystalline polymers [13,14]. In the parameter identification procedure, bigger weights for the first points of the plastic regime would allow us to identify parameters that describe properly this phenomenon, but would not capture accurately the overall hardening response.

5.1.2. Validation

Once the parameters are identified, the validation of the model is achieved using additional experimental results at different strain rates and temperatures. The comparison between experimental results, analytical calculations and numerical simulations is presented in Fig. 3.

For the model validation, experimental tensile tests have been conduced at three different temperatures (20 °C, 23 °C and 40 °C) and three different strain rates (24 s^{-1}, 27 s^{-1} and 258 s^{-1}). The analytical calculations and the numerical simulations exhibit the same stress-strain response and they are both very close to the experimental results. As expected, the model cannot capture accurately the stress softening response which appears during the transition between the elastic and the plastic regimes. As

mentioned in the identification part, the DSGZ model is fundamentally able to capture such softening characteristic for semi-crystalline polymers [13,14], but the parameter identification procedure followed here reduced this characteristic due to the equal weighting of all the points of the plastic regime. However, the maximum relative difference between the experimental and the simulated curves remains small and it is less than 8% in terms of stress in the worst case.

6. Numerical applications and model implementation capabilities

6.1. Application for tension-shear loading

In the previous section, the identification and the validation of the constitutive law are achieved using high speed tensile tests. In order to illustrate the capability of the developed numerical framework for multiaxial loading conditions, the proposed implicit implementation is applied to simulate tension-shear proportional loading paths at different rates and temperatures. Fig. 4 presents the influence of the temperature and the strain rate on the stress evolution of these tension-shear loading tests.

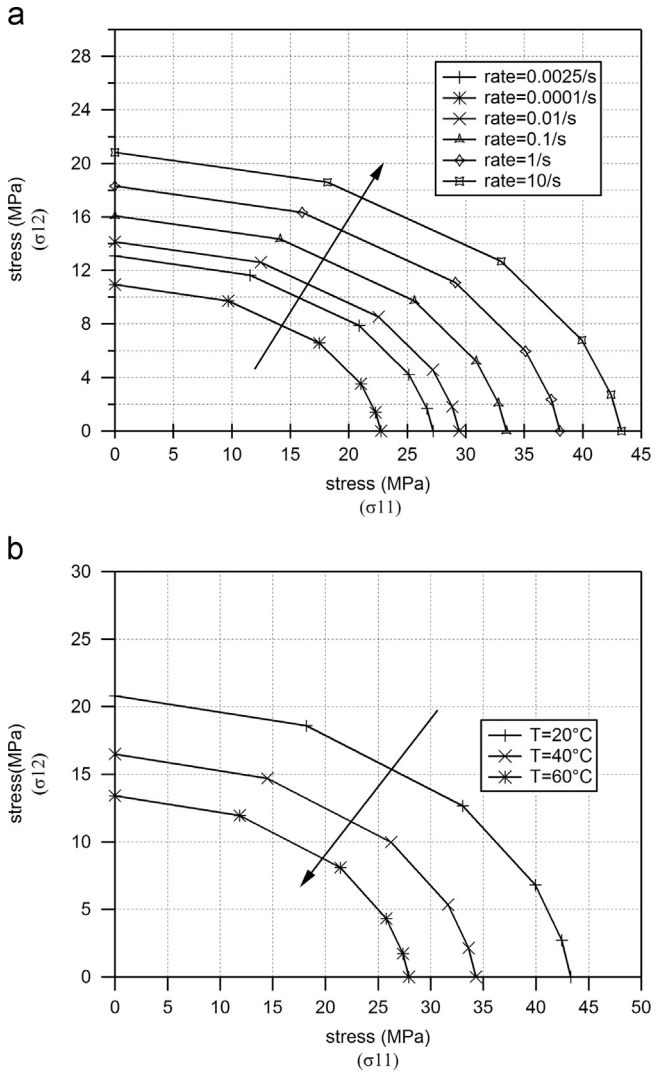

Fig. 4. Strain rate (a) and temperature (b) influence on stress evolution for tension-shear loading numerical tests.

Simulations have been conducted at 6 strain rates (from 1.10^{-4} s^{-1} to 10 s^{-1}) and 3 temperatures (20 °C, 40 °C and 60 °C). All the test cases have been performed above the glass transition temperature. For each curve, six tension/shear stress ratios have been chosen (0, 0.2, 0.4, 0.6, 0.8 and 1). The actual stress values are measured at 7% of total strain, which corresponds to a point in the plastic area. In Fig. 4, the shear stress is represented as a function of the tensile stress at different strain rates (Fig. 4_a) and at different temperatures (Fig. 4_b). The obtained curves form a load surface as a quarter ellipse in the range of positive tensile and shear stresses. The results are consistent and reflect the established effects of strain rate and temperature. Indeed, as expected, the load surface increases as the strain rate increases or the temperature decreases. Thus the numerical simulations show that the model is able to capture the multiaxial material behavior.

6.2. Structural FE analysis with the implicit implementation: impact loading

In the previous section, the capability of the DSZG model implementation to simulate a multiaxial behavior was demonstrated. The present section deals with an example of FE structural analysis using the implicit formulation to simulate the dynamic multiaxial response of a polymer disc subjected to an impact load. The simulation is performed according to the geometry defined in the ASTM D3763 standard for multiaxial impact test. The latter consists in dropping a cylindrical striker with hemispherical end onto a clamped polymer disc [14]. Fig. 5 shows the FE model of the multiaxial impact simulation used in ABAQUS/standard.

The striker is simulated using a rigid surface associated to a rigid body reference point. It moves along the vertical axis with a velocity of 2 m/s while the other degrees of freedom are set to zero. The polymer disc is considered as a viscoplastic solid and is discretized using 17,007 twenty-nodes quadratic brick elements with reduced integration (C3D20R). The external edge of the disc

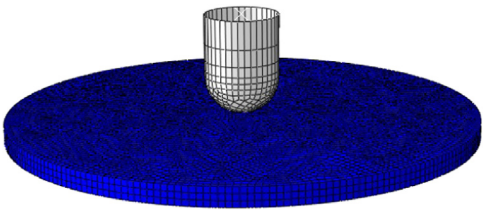

Fig. 5. FE model for ASTM D3763 multiaxial impact test.

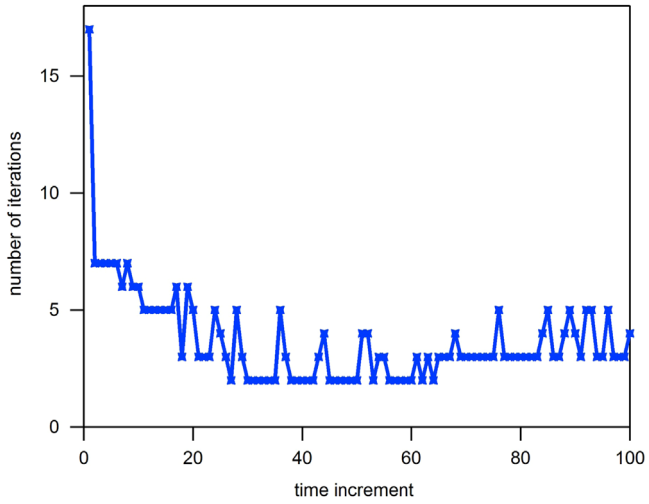

Fig. 6. Evolution of the number of iteration with the time increment.

is clamped. The general contact model of ABAQUS uses finite sliding with a friction coefficient between the striker and the disc. This coefficient is set equal to 0.0001. The material parameters for the polypropylene disc are given in Table 2. Computations are carried out for a total time of 0.002 s split in 100 equal time increments.

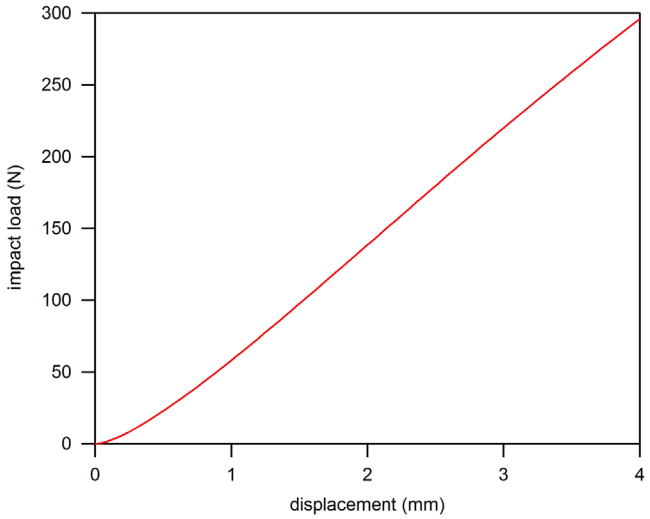

Fig. 7. Evolution of the impact load depending to the displacement.

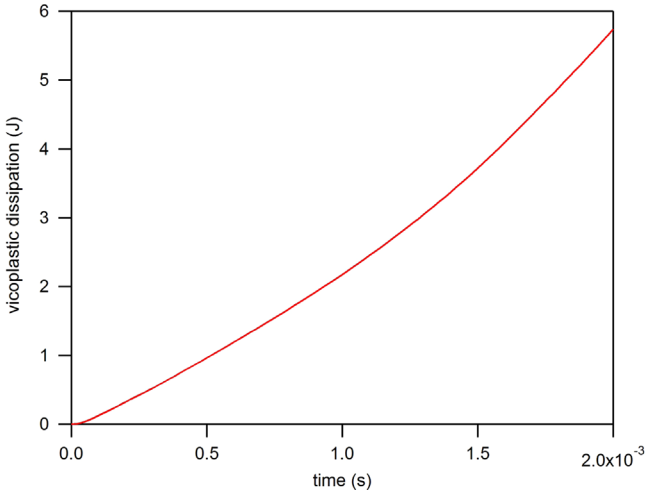

Fig. 8. Evolution of the viscoplastic dissipation.

As shown in Fig. 6, the number of local iterations decreases with the time very quickly to reach a minimum of 2 iterations for each time increment. Fig. 9 illustrates the computed equivalent Mises-stress distribution on the bottom of the polymer disc. The maximum stress is located at the center of the structure, as expected. Fig. 7 shows the evolution of the impact load as a function of the striker displacement. Fig. 8 gives the evolution of the viscoplastic dissipation with respect to time. Both these curves exhibit similar trend with the results obtained by Duan et al. [14] using explicit formulation.

7. Concluding remarks

In this paper a new, numerically implicit, three-dimensional formulation of the DSGZ model has been proposed. It has been implemented on the basis of the radial return mapping algorithm as an ABAQUS User Material. The material parameters of the model are identified on thermoplastic polypropylene. Three tensile tests at different rates and temperatures allows us to find the model parameters of this material using a Matlab genetic algorithm coupled with the Levenberg–Marquardt method. The simulation results are compared to the tensile tests at a range of strain rates from 0.92 s^{-1} to 258 s^{-1} and temperatures from 20 °C to 60 °C. A good agreement is observed between experiments and simulations. However, due to the parameter identification procedure (iso-weighting of all points in the plastic regime), the model does not capture accurately the stress softening response which appears during the transition between the elastic and the plastic regimes. Nevertheless, the maximum relative difference between the experimental and the simulated curves remains small (less than 8%), which is acceptable. The model has also been applied to simulate multiaxial proportional loading paths and to predict the material behavior under tension-shear loading at different strain rates and temperatures.

The advantage of the validated implicit formulation compared to previous explicit formulations in the literature is the determination of the consistent tangent modulus that allows multiscale modeling using an incremental micromechanical scale transition analysis, for instance the Mori–Tanaka scheme, where the constituents (matrix or inclusions) could have a thermoviscoplastic behavior. Finally, the model capability for structural computations has been illustrated through an impact loading numerical example. It has been shown that, at each time step, the implicit

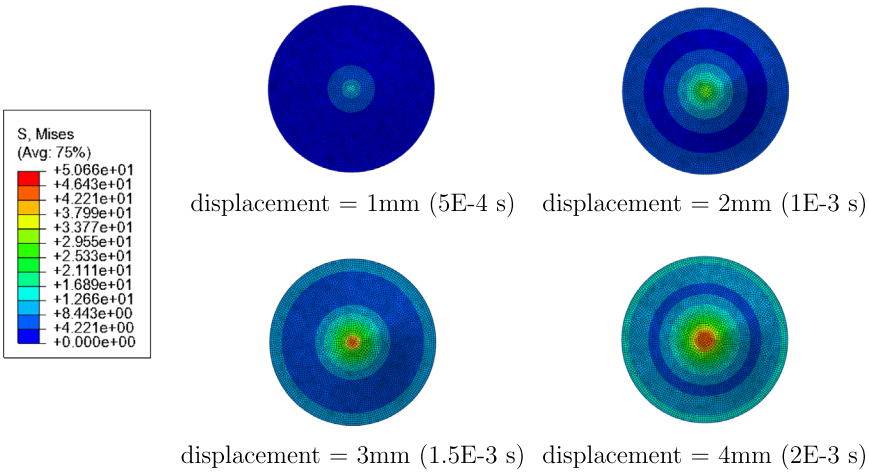

Fig. 9. Stress distribution on the bottom of the polymer disc.

formulation requires only a few iterations to achieve numerical convergence. In a future paper, this implementation will be included into a micromechanics scheme to predict the overall behavior of a composite consisting of a viscoplastic polypropylene as a matrix phase that behaves according to DSGZ model and short glass fibers as reinforcement.

Appendix A. Consistent tangent modulus for radial return mapping algorithm

The approach presented here for obtaining the consistent tangent modulus is similar to the one presented in [43] for elasto-plastic materials. For simplicity in the calculations, the indicial notation and the Einstein summation are utilized. The constitutive law is expressed in this way as

$$\begin{aligned}\Delta\sigma_{ij}^{(n+1)} &= 2\mu\Delta\varepsilon_{ij}^{(n+1)} + \left[\kappa - \frac{2}{3}\mu\right]\Delta\varepsilon_{kk}^{(n+1)}\delta_{ij} - 2\mu\Delta\varepsilon_{ij}^{p(n+1)} \\ &= 2\mu\Delta\varepsilon_{ij}^{(n+1)} + \left[\kappa - \frac{2}{3}\mu\right]\Delta\varepsilon_{kk}^{(n+1)}\delta_{ij} - 3\mu\eta_{ij}^{(n+1)}\dot{p}^{(n+1)}\Delta t.\end{aligned} \tag{A.1}$$

Taking the derivative with respect to $\Delta\varepsilon_{ij}^{(n+1)}$, yields

$$\begin{aligned}\frac{\partial\Delta\sigma_{ij}^{(n+1)}}{\partial\Delta\varepsilon_{kl}^{(n+1)}} &= 2\mu\frac{1}{2}[\delta_{il}\delta_{jk}+\delta_{ik}\delta_{jl}] + \left[\kappa - \frac{2}{3}\mu\right]\delta_{ij}\delta_{kl} - 3\mu\dot{p}^{(n+1)}\Delta t\frac{\partial\eta_{ij}^{(n+1)}}{\partial\Delta\varepsilon_{kl}^{(n+1)}} \\ &\quad - 3\mu\frac{\partial\dot{p}^{(n+1)}}{\partial\Delta\varepsilon_{kl}^{(n+1)}}\eta_{ij}^{(n+1)}\Delta t.\end{aligned} \tag{A.2}$$

Eq. $(20)_1$ gives

$$\frac{\partial\eta_{ij}^{(n+1)}}{\partial\Delta\varepsilon_{kl}^{(n+1)}} = \frac{\partial\eta_{ij}^{(n+1)}}{s_{pq}^{\mathrm{trial}(n+1)}}\frac{\partial s_{pq}^{\mathrm{trial}(n+1)}}{\partial\Delta\varepsilon_{kl}^{(n+1)}} = 2\mu\frac{\partial\eta_{ij}^{(n+1)}}{\partial s_{pq}^{\mathrm{trial}(n+1)}}\frac{\partial\Delta e_{pq}^{(n+1)}}{\partial\Delta\varepsilon_{kl}^{(n+1)}} \tag{A.3}$$

where

$$\frac{\Delta e_{pq}^{(n+1)}}{\partial\Delta\varepsilon_{kl}^{(n+1)}} = \frac{\partial\Delta\varepsilon_{pq}^{(n+1)}}{\partial\Delta\varepsilon_{kl}^{(n+1)}} - \frac{1}{3}\frac{\partial\Delta\varepsilon_{ii}^{(n+1)}}{\partial\Delta\varepsilon_{kl}^{(n+1)}}\delta_{pq} = \frac{1}{2}[\delta_{pl}\delta_{qk}+\delta_{pk}\delta_{ql}] - \frac{1}{3}\delta_{pq}\delta_{kl}. \tag{A.4}$$

Moreover,

$$\begin{aligned}\frac{\partial\eta_{ij}^{(n+1)}}{\partial s_{pq}^{\mathrm{trial}(n+1)}} &= \frac{\partial}{\partial s_{pq}^{\mathrm{trial}(n+1)}}\left(\frac{s_{ij}^{\mathrm{trial}(n+1)}}{\overline{\sigma}^{\mathrm{trial}(n+1)}}\right) \\ &= \frac{\frac{1}{2}[\delta_{ip}\delta_{jq}+\delta_{iq}\delta_{jp}]}{\overline{\sigma}^{\mathrm{trial}(n+1)}} - \frac{3}{2}s_{ij}^{\mathrm{trial}(n+1)}\frac{s_{kl}^{\mathrm{trial}(n+1)}\frac{1}{2}[\delta_{kp}\delta_{lq}+\delta_{kq}\delta_{lp}]}{\left[\overline{\sigma}^{\mathrm{trial}(n+1)}\right]^3} \\ &= \frac{1}{\overline{\sigma}^{\mathrm{trial}(n+1)}}\left[\frac{1}{2}[\delta_{ip}\delta_{jq}+\delta_{iq}\delta_{jp}] - \frac{3}{2}\eta_{ij}^{(n+1)}\eta_{pq}^{(n+1)}\right].\end{aligned} \tag{A.5}$$

Using Eqs. (A.4) and (A.5), Eq. (A.3) is written

$$\begin{aligned}\frac{\partial\eta_{ij}^{(n+1)}}{\partial\Delta\varepsilon_{kl}^{(n+1)}} &= \frac{2\mu}{\overline{\sigma}^{\mathrm{trial}(n+1)}}\left[\frac{1}{2}[\delta_{pl}\delta_{qk}+\delta_{pk}\delta_{ql}] - \frac{1}{3}\delta_{pq}\delta_{kl}\right] \\ &\quad\times\left[\frac{1}{2}[\delta_{ip}\delta_{jq}+\delta_{iq}\delta_{jp}] - \frac{3}{2}\eta_{ij}^{(n+1)}\eta_{pq}^{(n+1)}\right] \\ &= \frac{2\mu\left[\frac{1}{2}[\delta_{il}\delta_{jk}+\delta_{ik}\delta_{jl}] - \frac{1}{3}\delta_{ij}\delta_{kl}\right] - 3\mu\eta_{ij}^{(n+1)}\eta_{kl}^{(n+1)}}{\overline{\sigma}^{\mathrm{trial}(n+1)}}.\end{aligned} \tag{A.6}$$

The final result of Eq. (A.6) holds, because the term $\eta_{ij}^{(n+1)}\eta_{pp}^{(n+1)}\delta_{kl}$ is zero. Differentiating the numerical form of the yield criterion Eq. $(23)_1$ with respect to the total strain increment, yields

$$\frac{\partial\Phi^{p(n+1)}}{\partial\Delta\varepsilon_{kl}^{(n+1)}} = \frac{\partial\overline{\sigma}^{\mathrm{trial}(n+1)}}{\partial\Delta\varepsilon_{kl}^{(n+1)}} - 3\mu\frac{\dot{p}^{(n+1)}}{\partial\Delta\varepsilon_{kl}^{(n+1)}}\Delta t - \frac{\partial\sigma_y^{(n+1)}}{\partial p^{(n+1)}}\frac{\partial p^{(n+1)}}{\partial\Delta\varepsilon_{kl}^{(n+1)}}$$

$$-\frac{\partial\sigma_y^{(n+1)}}{\partial\dot{p}^{(n+1)}}\frac{\partial\dot{p}^{(n+1)}}{\partial\Delta\varepsilon_{kl}^{(n+1)}} = 0. \tag{A.7}$$

From Eq. $(23)_2$ holds

$$\frac{\partial p^{(n+1)}}{\partial\Delta\varepsilon_{kl}^{(n+1)}} = \frac{\partial\dot{p}^{(n+1)}}{\partial\Delta\varepsilon_{kl}^{(n+1)}}\Delta t.$$

Moreover, using Eqs. $(20)_1$ and (A.4) yields

$$\frac{\partial\overline{\sigma}^{\mathrm{trial}(n+1)}}{\partial\Delta\varepsilon_{kl}^{(n+1)}} = \frac{2\frac{3}{2}s_{pq}^{\mathrm{trial}(n+1)}\frac{\partial s_{pq}^{\mathrm{trial}(n+1)}}{\partial\Delta\varepsilon_{kl}^{(n+1)}}}{2\overline{\sigma}^{\mathrm{trial}(n+1)}} = 3\mu\frac{s_{kl}^{\mathrm{trial}(n+1)}}{\overline{\sigma}^{\mathrm{trial}(n+1)}} = 3\mu\eta_{kl}^{(n+1)}.$$

Thus Eq. (A.7) leads to

$$\frac{\dot{p}^{(n+1)}}{\partial\Delta\varepsilon_{kl}^{(n+1)}} = \frac{\eta_{kl}^{(n+1)}}{\left[1+\frac{1}{3\mu}\frac{\partial\sigma_y^{(n+1)}}{\partial p^{(n+1)}}\right]\Delta t + \frac{1}{3\mu}\frac{\partial\sigma_y^{(n+1)}}{\partial\dot{p}^{(n+1)}}}. \tag{A.8}$$

Finally, using Eqs. (A.6) and (A.8), the consistent tangent modulus Eq. (A.2) is written

$$\begin{aligned}\frac{\partial\Delta\sigma_{ij}^{(n+1)}}{\partial\Delta\varepsilon_{kl}^{(n+1)}} &= \kappa\delta_{ij}\delta_{kl} + 2\mu\left[1 - \frac{3\mu\dot{p}^{(n+1)}\Delta t}{\overline{\sigma}^{\mathrm{trial}(n+1)}}\right]\left[\frac{1}{2}[\delta_{il}\delta_{jk}+\delta_{ik}\delta_{jl}] - \frac{1}{3}\delta_{ij}\delta_{kl}\right] \\ &\quad - 3\mu\left[\frac{\Delta t}{\left[1+\frac{1}{3\mu}\frac{\partial\sigma_y^{(n+1)}}{\partial p^{(n+1)}}\right]\Delta t + \frac{1}{3\mu}\frac{\partial\sigma_y^{(n+1)}}{\partial\dot{p}^{(n+1)}}} - \frac{3\mu\dot{p}^{(n+1)}\Delta t}{\overline{\sigma}^{\mathrm{trial}(n+1)}}\right]\eta_{ij}^{(n+1)}\eta_{kl}^{(n+1)},\end{aligned} \tag{A.9}$$

and using Eq. $(23)_1$, the final form Eq. (24) is obtained.

References

[1] Abdul-Hameed H, Messager T, Zairi F, Nait-Abdelaziz M. Large-strain viscoelastic-viscoplastic constitutive modeling of semi-crystalline polymers and model identification by deterministic/evolutionary approach. Comput Mater Sci 2014;90:241–52.

[2] Arif M, Meraghni F, Chemisky Y, Despringre N, Robert G. In situ damage mechanisms investigation of PA66/GF30 composite: effect of relative humidity. Compos Part B: Eng 2014;58:487–95.

[3] Ayoub G, Zairi F, Nait-Abdelaziz M, Gloaguen J. Modelling large deformation behaviour under loading-unloading of semicrystalline polymers: application to a high density polyethylene. Int J Plast 2010;26(3):329–47.

[4] Balieu R, Lauro F, Bennani B, Delille R, Matsumoto T, Mottola E. A fully coupled elastoviscoplastic damage model at finite strains. Int J Plast 2013;51:241270.

[5] Billon N. New constitutive modeling for time-dependent mechanical behavior of polymers close to glass transition: fundamentals and experimental validation. J Appl Polym Sci 2012;125(6):4390–401.

[6] Brooks J. Thermo-mechanical processing: theory, modeling and practice. In: A conference organized in celebration of the 75th anniversary of the Swedish Society for Material Technology; 1996.

[7] Brostow W, Corneliussen R. Failure of plastics. New York: Macmillan Pub.; 1986.

[8] Chemisky Y, Meraghni F, Bourgeois N, Cornell S, Echchorfi R, Patoor E. Analysis of the deformation paths and thermomechanical parameter identification of a shape memory alloy using digital image correlation over heterogeneous tests. Int J Mech Sci 2015;9697(0):13–24.

[9] Chen WF, Han DJ. Plasticity for structural engineers. Berlin: Springer; 1988.

[10] Colak O. Modeling deformation behavior of polymers with viscoplasticity theory based on overstress. Int J Plast 2005;21(1):145–60.

[11] Doghri I, Ouaar A. Homogenization of two-phase elasto-plastic composite materials and structures. Study of tangent operators, cyclic plasticity and structures. Int J Solids Struct 2003;40:1681–712.

[12] Drozdov, Christiansen J. Thermo-viscoleastic and viscoplastic behaviour of high-density polyethylene. Int J Solids Struct 2008;45:4274–88.

[13] Duan Y, Saigal A, Greif R, Zimmerman MA. A uniform phenomenological constitutive model for glassy and semicrystalline polymers. Polym Eng Sci 2001;41(8):1322–8.

[14] Duan Y, Saigal A, Greif R, Zimmerman MA. Analysis of multiaxial impact behavior of polymers. Polym Eng Sci 2002;42(2):395–402.

[15] Fleischhauer R, Dal H, Kaliske M, Schneider K. A constitutive model for finite deformation of amorphous polymers. Int J Mech Sci 2012;65(1):48–63.

[16] Ghorbel E. A viscoplastic constitutive model for polymeric materials. Int J Plast 2008;24:20322058.
[17] G'Sell C, Jonas J. Determination of the plastic behaviour of solid polymer at constant true strain rate. J Mater Sci 1979;14:583–91.
[18] G'Sell C, Jonas J. Yield and transient effects during the plastic deformation of solid polymers. J Mater Sci 1981;16:1956–74.
[19] Hartl DJ, Chatzigeorgiou G, Lagoudas DC. Three-dimensional modeling and numerical analysis of rate-dependent irrecoverable deformation in shape memory alloys. Int J Plast 2010;26(10):1485–507.
[20] Hartl DJ, Lagoudas DC. Constitutive modeling and structural analysis considering simultaneous phase transformation and plastic yield in shape memory alloys. Smart Mater Struct 2009;18:1–17.
[21] Hasan O, Boyce M. Constitutive model for the nonlinear viscoelastic viscoplastic behavior of glassy polymers. Polym Eng Sci 1995;35(4):331–44.
[22] Haupt P, Lion A, Backhaus E. On the dynamic behaviour of polymers under finite strains: constitutive modelling and identification of parameters. Int J Solids Struct 2000;37(26):3633–46.
[23] Holmes D, Loughran J, Suehrcke H. Constitutive model for large strain deformation of semicrystalline polymers. Mech Time-Depend Mater 2006;10 (4):281–313.
[24] Hughes TJ, Winget J. Finite rotation effects in numerical integration of rate constitutive equations arising in large-deformation analysis. Int J Numer Methods Eng 1980;15(12):1862–7.
[25] Jendli Z, Fitoussi J, Meraghni F, Baptiste D. Anisotropic strain rate effects on the fibre-matrix interface decohesion in sheet moulding compound composites. Compos Sci Technol 2005;65(3–4):387–93.
[26] Jendli Z, Meraghni F, Fitoussi J, Baptiste D. Multi-scales modelling of dynamic behaviour for discontinuous fibre SMC composites. Compos Sci Technol 2009;69(1):97–103.
[27] Johnson G, Cook W. A constitutive model and data for metals subjected to large strains, high strain rates, and high temperatures. In: 7th International Symposium on Ballistics; 1983.
[28] Kästner M, Obst M, Brummund J, Thielsch K, Ulbricht V. Inelastic material behavior of polymers—experimental characterization, formulation and implementation of a material model. Mech Mater 2012;52:40–57.
[29] Khan A, Lopez-Pamies O, Kazmi R. Thermo-mechanical large deformation response and constitutive modeling of viscoelastic polymers over a wide range of strain rates and temperatures. Int J Plast 2006;22(4):581–601.
[30] Khan AS, Huang S. Continuum theory of plasticity. New York: John Wiley & Sons, Inc.; 1995.
[31] Kim J, Muliana A. A time-integration method for the viscoelastic–viscoplastic analyses of polymers and finite element implementation. Int J Numer Methods Eng 2009;79(5):550–75.
[32] Kweon S, Benzerga A. Finite element implementation of a macromolecular viscoplastic polymer model. Int J Numer Methods Eng 2013;94(10):895–919.
[33] Lemaitre J, Chaboche JL. Mechanics of solid materials. Cambridge, UK: Cambridge University Press; 2002.
[34] Meraghni F, Chemisky Y, Piotrowski B, Echchorfi R, Bourgeois N, Patoor E. Parameter identification of a thermodynamic model for superelastic shape memory alloys using analytical calculation of the sensitivity matrix. Eur J Mech A/Solids 2014;45:226–37.
[35] Miehe C, Méndez Diez J, Göktepe S, Schänzel L-M. Coupled thermo-viscoplasticity of glassy polymers in the logarithmic strain space based on the free volume theory. Int J Solids Struct 2011;48(13):1799–817.
[36] Miled B, Doghri I, Delannay L. Coupled viscoelastic–viscoplastic modeling of homogeneous and isotropic polymers: numerical algorithm and analytical solutions. Comput Methods Appl Mech Eng 2011;200(4748):3381–94.
[37] Nouri H, Meraghni F, Lory P. Fatigue damage model for injection-molded short glass fibre reinforced thermoplastics. Int J Fatigue 2009;31(5):934–42.
[38] Ortiz M, Simo JC. An analysis of a new class of integration algorithms for elastoplastic constitutive relations. Int J Numer Methods Eng 1986;23:353–66.
[39] Pouriayevali H, Arabnejad S, Guo Y, Shim V. A constitutive description of the rate-sensitive response of semi-crystalline polymers. Int J Impact Eng 2013;62:35–47.
[40] Pyrz M, Zairi F. Identification of viscoplastic parameters of phenomenological constitutive equations for polymers by deterministic and evolutionary approach. Model Simul Mater Sci Eng 2007;15(2):85.
[41] Qidwai MA, Lagoudas DC. Numerical implementation of a shape memory alloy thermomechanical constitutive model using return mapping algorithms. Int J Numer Methods Eng 2000;47:1123–68.
[42] Rafsanjani A. Writing User Subroutines with ABAQUS; 2010. Source: Online since 2010-02-11, ⟨http://imechanica.org/⟩.
[43] Simo JC, Hughes TJR. Computational inelasticity. New York, USA: Springer-Verlag; 1998.